
This is an electronic reprint of the original article.
This reprint may differ from the original in pagination and typographic detail.

Perrott, Yvette C.; Lopez-Caniego, Marcos; Genova-Santos, Ricardo T.; Rubino-Martin, Jose Alberto; Ashdown, Mark; Herranz, Diego; Lahteenmaki, Anne; Lasenby, Anthony N.; Lopez-Caraballo, Carlos H.; Poidevin, Frederick; Tornikoski, Merja
28-40 GHz variability and polarimetry of bright compact sources in the QUIJOTE cosmological fields

Published in:
Monthly Notices of the Royal Astronomical Society

DOI:
[10.1093/mnras/stab400](https://doi.org/10.1093/mnras/stab400)

Published: 01/04/2021

Document Version
Publisher's PDF, also known as Version of record

Please cite the original version:
Perrott, Y. C., Lopez-Caniego, M., Genova-Santos, R. T., Rubino-Martin, J. A., Ashdown, M., Herranz, D., Lahteenmaki, A., Lasenby, A. N., Lopez-Caraballo, C. H., Poidevin, F., & Tornikoski, M. (2021). 28-40 GHz variability and polarimetry of bright compact sources in the QUIJOTE cosmological fields. *Monthly Notices of the Royal Astronomical Society*, 502(4), 4779-4793. <https://doi.org/10.1093/mnras/stab400>

This material is protected by copyright and other intellectual property rights, and duplication or sale of all or part of any of the repository collections is not permitted, except that material may be duplicated by you for your research use or educational purposes in electronic or print form. You must obtain permission for any other use. Electronic or print copies may not be offered, whether for sale or otherwise to anyone who is not an authorised user.

28–40 GHz variability and polarimetry of bright compact sources in the QUIJOTE cosmological fields

Yvette C. Perrott ^{1,2}★ Marcos López-Caniego,³ Ricardo T. Génova-Santos,^{4,5}
Jose Alberto Rubiño-Martín,^{4,5} Mark Ashdown,^{1,6} Diego Herranz,⁷ Anne Lähteenmäki,^{8,9}
Anthony N. Lasenby,^{1,6} Carlos H. López-Caraballo,^{4,5,10} Frédéric Poidevin^{4,5} and Merja Tornikoski⁸

¹*Astrophysics Group, Cavendish Laboratory, JJ Thomson Avenue, Cambridge CB3 0HE, UK*

²*School of Chemical and Physical Sciences, Victoria University of Wellington, PO Box 600, Wellington 6140, New Zealand*

³*European Space Agency, ESAC, Camino bajo del Castillo, s/n, Urbanización Villafranca del Castillo, Villanueva de la Cañada, E-28692 Madrid, Spain*

⁴*Instituto de Astrofísica de Canarias (IAC), E-38205 La Laguna, Tenerife, Spain*

⁵*Dpto. Astrofísica, Universidad de La Laguna, E-38206 La Laguna, Tenerife, Spain*

⁶*Kavli Institute for Cosmology, University of Cambridge, Madingley Road, Cambridge CB3 0HA, UK*

⁷*Instituto de Física de Cantabria (CSIC-Universidad de Cantabria), Avda. de los Castros s/n, E-39005 Santander, Spain*

⁸*Aalto University Metsähovi Radio Observatory, Metsähovintie 114, FI-02540 Kylmälä, Finland*

⁹*Aalto University Department of Electronics and Nanoengineering, PO Box 15500, FI-00076 Aalto, Finland*

¹⁰*INFN Sezione di Milano, Via Celoria 16, I-20133 Milano, Italy*

Accepted 2021 February 2. Received 2021 February 1; in original form 2020 February 3

ABSTRACT

We observed 51 sources in the Q-U-I JOint TEnerife (QUIJOTE) cosmological fields that were brighter than 1 Jy at 30 GHz in the *Planck* Point Source Catalogue (version 1), with the Very Large Array at 28–40 GHz, in order to characterize their high-radio-frequency variability and polarization properties. We find a roughly lognormal distribution of polarization fractions with a median of 2 per cent, in agreement with previous studies, and a median rotation measure (RM) of $\approx 1110 \text{ rad m}^{-2}$ with one outlier up to $\approx 64\,000 \text{ rad m}^{-2}$, which is among the highest RMs measured in quasar cores. We find hints of a correlation between the total intensity flux density and median polarization fraction. We find 59 per cent of sources are variable in total intensity, and 100 per cent in polarization at 3σ level, with no apparent correlation between total intensity variability and polarization variability. This indicates that it will be difficult to model these sources without simultaneous polarimetric monitoring observations and they will need to be masked for cosmological analysis.

Key words: quasars: general – cosmic background radiation – cosmology: observations – radio continuum: general.

1 INTRODUCTION

The Q-U-I JOint TEnerife (QUIJOTE) experiment (Rubiño-Martín et al. 2010) aims to detect inflationary B modes using CMB observations at 31 and 42 GHz with supporting observations between 10 and 20 GHz to characterize foregrounds. The low angular resolution ($\approx 1^\circ$) of the instrument means that polarized extragalactic radio sources, a major contaminant at small angular scales (e.g. Puglisi et al. 2018), cannot be accurately characterized by the experiment and ancillary data must be used to either subtract or mask them. Ideally, these sources would be monitored at higher resolution simultaneously with the cosmological observations as for the Very Small Array experiment (Grainge et al. 2003), however since this was not possible we investigated the long-term properties of the bright sources in the field to assess the level of contamination an inaccurate subtraction would introduce. The polarization and variability properties of radio sources at these frequencies are not well studied; some of the relevant existing studies are listed in Table 1. Polarimetric very-long-baseline interferometric monitoring studies exist at 43 GHz, e.g. Park et al. (2018), Algaba, Gabuzda & Smith 2011, 2012, Jorstad et al.

(2007), and Lister (2001); however these focus on spatially resolving properties of the sources rather than investigating their integrated properties, which are of relevance to experiments such as QUIJOTE. At the other end of the resolution scale, Bonavera et al. (2017) stack *Planck* data to statistically detect polarization from known source positions and constrain average polarization properties, but are too limited by sensitivity to investigate variability. Galluzzi & Massardi (2016) and Galluzzi et al. (2017, 2018) detect a large sample of sources between 2 and 38 GHz; however, they only have repeated observations for a small subsample of sources and focus on broadband polarimetry rather than variability. It is clear that there are very few studies addressing the integrated variability of bright, polarized sources at 30–40 GHz; we therefore observed the brightest sources in the QUIJOTE fields using the Very Large Array (VLA) to determine at what level in intensity a source could be safely subtracted in polarization.

This paper is organized as follows. In Section 2, we introduce our sample; in Section 3, we describe our observations, data reduction, and analysis methods. In Section 4, we summarize our results and investigate correlations between the measured quantities. In Section 5, we investigate in more detail some interesting or anomalous cases. In Section 6, we discuss implications for QUIJOTE, and in Section 7, we conclude.

* E-mail: yvette.perrott@vuw.ac.nz

Table 1. Characteristics of polarimetric studies of radio sources at frequencies overlapping the 30–40 GHz band of this study.

Reference	Instrument	Frequencies	Epochs	Number of sources	Comment
Rudnick et al. (1985), Jones et al. (1985)	1.4–90 GHz (eight bands)	Kitt Peak 10.6 m (for 31 GHz)	Six total, two at 31 GHz	≈20	Strong, flat-spectrum sources
López-Caniego et al. (2009)	WMAP	23, 33, 41, 61 GHz	Single 5-yr average	41 (30) at 99 per cent significance at 33 (41) GHz	Survey maps correlated with total intensity source catalogue
Jackson et al. (2010), Battye et al. (2011)	VLA	8, 22, 43 GHz	1	203	Brighter than 1 Jy in the WMAP 22-GHz catalogue
Sajina et al. (2011)	VLA	4, 8, 22, 43 GHz	1 at 4, 8, 43 GHz; 2 at 22 GHz	159	Radio galaxies with Australia Telescope 20-GHz (AT20G) survey flux densities >40 mJy in Atacama Cosmology Telescope cosmological field
Kravchenko, Cotton & Kovalev (2015)	VLA	1.4–43 GHz (8 bands)	3	7	Bright calibration sources
Huffenberger et al. (2015)	Q/U Imaging Experiment	43, 95 GHz	Single 25-month average	13 at S/N>2.7 at 43 GHz	Survey maps correlated with AT20G sources
Galluzzi & Massardi (2016), Galluzzi et al. (2017), Galluzzi et al. (2018)	ATCA	2–38 GHz	2 in polarization for 10 sources	104	‘Faint’ Planck-ATCA Coeval Observation sample, >200 mJy at 20 GHz, Southern Ecliptic Pole region
Bonavera et al. (2017), Planck Collaboration XXVI (2016)	Planck	30–353 GHz	4 yr, averaged	1560 (stacked)	PCCS2 30-GHz sources >427 mJy

Throughout this paper, we will use the following conventions. When fitting a power law as a function of frequency, we will use the convention $S \propto \nu^\alpha$ (i.e. $\alpha > 0$ means a rising function of frequency). For polarization, we will use \mathcal{I} , \mathcal{Q} , \mathcal{U} to denote flux density in total intensity and Stokes Q and U, respectively. We will use $q = \mathcal{Q}/\mathcal{I}$ and $u = \mathcal{U}/\mathcal{I}$ to indicate the fractional quantities and similarly $\mathcal{P} = \sqrt{\mathcal{Q}^2 + \mathcal{U}^2}$ and $p = \mathcal{P}/\mathcal{I}$ to denote the total and fractional linear polarization. Polarization angle will be indicated as Φ , i.e. $\tan(2\Phi) = u/q$. Circular polarization will be assumed to be zero throughout.

2 SAMPLE PROPERTIES

We selected the 54 sources with flux densities greater than 1 Jy at 30 GHz in the first *Planck* Catalogue of Compact Sources (PCCS1; Planck Collaboration XXVIII 2014) lying within 30° of the centres of the three QUIJOTE cosmological fields at RA, $\delta = (00^{\text{h}}40^{\text{m}}, +25^\circ)$, $(09^{\text{h}}40^{\text{m}}, +45^\circ)$ and $(16^{\text{h}}20^{\text{m}}, +50^\circ)$, respectively. We note that the second, more-complete version of the catalogue (PCCS2; Planck Collaboration XXVI 2016) was not available at the time of sample selection; however, completeness is not an issue for this high signal-to-noise ratio (SNR) sample since at 30 GHz PCCS1 is estimated to be 90 per cent complete at 575 mJy. Had we selected from PCCS2, ≈ 10 per cent of the sample would have been different due to the source flux densities varying over/under the 1-Jy threshold.

Three of the sources in the sample were excluded due to large angular size, leaving a sample of 51 that were observed with the VLA at frequencies between 28 and 40 GHz, with 41 sources having two epochs of observation. The sources, as expected given the high-frequency selection, are mostly blazars and have identifications in the fifth edition of the Roma-BZCAT Multifrequency Catalogue of Blazars (Massaro et al. 2015); these are listed in Table 2 along with coordinates and other identifications taken from the SIMBAD Astronomical Database.¹ The two sources not in the BZCAT are a LINER-type AGN and a Seyfert-1 galaxy.

¹<http://simbad.u-strasbg.fr/simbad/>.

3 OBSERVATIONS AND DATA REDUCTION

The sources were observed on the dates listed in Table 3. Observations were carried out with a custom correlator configuration that allowed simultaneous observing at two frequency bands, 28.5–32.4 and 35.5–39.4 GHz. Each band was then divided into 32 spectral windows, each with 64 channels of 2 MHz width.

We used either 3C 286 or 3C 48 as the flux density calibrator, both in total intensity and polarization, depending on which was closer in the sky to the sources being observed. In the case of 3C 286, we used J1407+2827 as the polarization leakage calibrator; in the case of 3C 48, we used 3C 84. These are both recommended as primary low polarization leakage calibrators for the VLA (<https://science.nrao.edu/facilities/vla/docs/manuals/obsguide/modes/pol>; see table 7.2.3). Since these sources are blazars, their emission at these frequencies is dominated by the compact core and they can be treated to a good approximation as point sources. We therefore used the targets themselves as phase calibrators, and performed pointing calibration scans at X band throughout the observations on targets less than 20° from the subsequent scans.

The data reduction was performed in CASA 5.3.0 and was based on the standard VLA data reduction pipeline adapted for our observations. As in the pipeline, we use the standard flux calibration sources 3C 48 or 3C 286 to calculate delay and bandpass calibrations. Departing from the pipeline, we then assume a point source model for each of the target sources and self-calibrate them in amplitude and phase. We use the ‘fluxscale’ task to translate the amplitude solutions into a spectral fit for each target source; see Fig. 3 for an example fit).

To check that our point source model accurately describes the sources, we subtract the model from the calibrated data and inspect the residual maps and visibilities. In most cases, the residuals are <1 per cent of the core flux density. In the few cases that the residuals are larger, we iteratively improve the model by adding in the non-core flux observed on the map, then solving again for the core flux density in the updated core + non-core model. Maps and uv -plane residuals are shown for all sources in Appendix A (available as supplementary material).

Table 2. Sources in the sample, positions, and associations taken from SIMBAD, classifications taken from BZCAT (Massaro et al. 2015).

PCCS1 030	z	RA	Dec.	Name	Class	Comment
G107.00–50.62	0.089	00:10:31.01	+10:58:29.5	5BZQ J0010+1058	FSRQ	Mrk 1501 (Sy1)
G115.13–64.85	0.21968 ^a	00:38:20.53	–02:07:40.5			3C 17 (resolved)
G124.55–32.50	0.016485 ^b	00:57:48.89	+30:21:08.8			NGC 315 (LIN)
G131.84–60.98	2.099	01:08:38.77	+01:35:00.3	5BZQ J0108+0135	FSRQ	4C 01.02, [V2003b] QSO J0108+0135 (QSO with absorption lines)
G129.46–49.29	0.05970 ^c	01:08:52.87	+13:20:14.3			3C 33 (resolved)
G134.59–50.34	0.57	01:21:41.60	+11:49:50.4	5BZQ J0121+1149	FSRQ	QSO B0119+115
G129.09–13.46	0.067	01:28:08.06	+49:01:06.0	5BZG J0128+4901	BL Lac-galaxy dominated	2MASX J01280804+4901056 (Sy1)
G130.78–14.31	0.859	01:36:58.59	+47:51:29.1	5BZQ J0136+4751	FSRQ	QSO B0133+476
G141.09–38.56	1.32	01:52:18.06	+22:07:07.7	5BZQ J0152+2207	FSRQ	QSO B0149+218
G147.84–44.04	0.833	02:04:50.41	+15:14:11.0	5BZU J0204+1514	Blazar Uncertain type	4C 15.05 (blazar)
G140.56–28.12	1.466	02:05:04.93	+32:12:30.1	5BZQ J0205+3212	FSRQ	7C 020209.69+315812.00 (QSO)
G152.57–47.29	0.20 ^d	02:11:13.18	+10:51:34.8	5BZB J0211+1051	BL Lac	2MASS J02111317+1051346 (BLL)
G140.23–16.73	0.021258 ^e	02:23:11.41	+42:59:31.4			UGC 1841 (Sy1)
G157.08–42.72	2.065	02:31:45.89	+13:22:54.7	5BZQ J0231+1322	FSRQ	4C 13.14, [RKV2003] QSO J0231+1322 (QSO with absorption lines)
G149.50–28.53	1.206	02:37:52.41	+28:48:09.0	5BZQ J0237+2848	FSRQ	4C 28.07 (QSO)
G156.86–39.13	0.94	02:38:38.93	+16:36:59.3	5BZB J0238+1636	BL Lac	[RKV2003] QSO J0238+1637, QSO B0235+1624, [CGK2006] QSO 0235+164 –00.33–0.45 (QSO with ALS, BLL, G?)
G178.26+33.40	0.53	08:18:16.00	+42:22:45.4	5BZB J0818+4222	BL Lac	7C 081451.89+423206.00 (BLL)
G182.17+34.17	1.216	08:24:55.48	+39:16:41.9	5BZQ J0824+3916	FSRQ	4C 39.23A (QSO)
G200.04+31.88	0.939	08:30:52.09	+24:10:59.8	5BZQ J0830+2410	FSRQ	[RKV2003] QSO J0830+2411, 7C 082754.29+242103.00 (QSO with absorption lines)
G143.53+34.42	2.218	08:41:24.36	+70:53:42.2	5BZQ J0841+7053	FSRQ	7C 083620.60+710405.00, [TOS2004] QSO J0841+7053 (QSO with absorption lines)
G206.82+35.81	0.306	08:54:48.87	+20:06:30.6	5BZB J0854+2006	BL Lac	QSO J0854+2006 (BLL)
G175.72+44.81	2.19	09:20:58.46	+44:41:54.0	5BZQ J0920+4441	FSRQ	7C 091741.89+445438.00 (QSO)
G152.23+41.00	1.446	09:21:36.23	+62:15:52.2	5BZQ J0921+6215	FSRQ	7C 091740.39+622838.00 (QSO)
G198.82+44.43	0.744	09:23:51.52	+28:15:25.0	5BZQ J0923+2815	FSRQ	9C J0923+2815 (QSO)
G183.71+46.17	0.695	09:27:03.01	+39:02:20.9	5BZQ J0927+3902	FSRQ	ICRF J092703.0+390220 (Sy1)
G181.02+50.29	1.249	09:48:55.34	+40:39:44.6	5BZQ J0948+4039	FSRQ	7C 094550.20+405345.00 (QSO)
G141.43+40.58	0.000677 ^f	09:55:52.73	+69:40:45.8			M82 (resolved)
G145.78+43.13	0.367	09:58:47.25	+65:33:54.8	5BZB J0958+6533	BL Lac	7C 095457.89+654812.00 (BLL)
G177.37+58.35	1.117	10:33:03.71	+41:16:06.2	5BZQ J1033+4116	FSRQ	7C 103008.00+413135.00 (QSO)
G211.56+60.99	0.56	10:43:09.03	+24:08:35.4	5BZQ J1043+2408	FSRQ	2MASS J10430901+2408354 (BLL)
G135.47+42.26	1.15	10:48:27.62	+71:43:35.9	5BZU J1048+7143	Blazar Uncertain type	7C 104450.00+715929.00 (QSO)
G135.91+43.92	2.492	10:56:53.62	+70:11:45.9	5BZQ J1056+7011	FSRQ	7C 105328.60+702751.00 (QSO)
G133.79+42.34	1.462	11:01:48.81	+72:25:37.1	5BZQ J1101+7225	FSRQ	7C 105819.89+724145.00 (QSO)
G174.43+69.81	1.733	11:30:53.28	+38:15:18.5	5BZQ J1130+3815	FSRQ	QSO B1128+385 (QSO)
G145.65+64.96	0.334	11:53:24.47	+49:31:08.8	5BZQ J1153+4931	FSRQ	7C 115048.00+494751.00 (QSO)
G098.27+58.31	0.153	14:19:46.60	+54:23:14.8	5BZB J1419+5423	BL Lac	7C 141805.29+543657.00 (BLL)
G105.20+49.72	2.068	14:36:45.80	+63:36:37.9	5BZQ J1436+6336	FSRQ	[RKV2003] QSO J1436+6336, 8C 1435+638, [TOS2004] QSO J1436+6336 (QSO with absorption lines)
G055.14+46.37	1.397	16:13:41.06	+34:12:47.9	5BZQ J1613+3412	FSRQ	7C 161147.89+342019.00 (QSO)
G061.07+42.34	1.814	16:35:15.49	+38:08:04.5	5BZQ J1635+3808	FSRQ	[V2003b] QSO J1635+3808, 7C 163330.69+381410.00 (QSO with absorption lines)
G073.40+41.88	0.735	16:37:45.13	+47:17:33.8	5BZQ J1637+4717	FSRQ	7C 163619.69+472344.00 (QSO)
G086.64+40.35	0.751	16:38:13.46	+57:20:24.0	5BZQ J1638+5720	FSRQ	ICRF J163813.4+572023 (Sy1)
G100.68+36.62	0.751	16:42:07.85	+68:56:39.7	5BZQ J1642+6856	FSRQ	6C 164218+690201 (QSO)
G063.46+40.96	0.593	16:42:58.81	+39:48:37.0	5BZQ J1642+3948	FSRQ	3C 345, 7C 164117.60+395412.00 (QSO)
G071.46+33.28	0.717	17:27:27.65	+45:30:39.7	5BZQ J1727+4530	FSRQ	ICRF J172727.6+453039 (Sy1)
G064.03+31.01	0.976	17:34:20.58	+38:57:51.4	5BZQ J1734+3857	FSRQ	7C 173240.70+385949.00 (BLL)
G079.56+31.72	1.381	17:40:36.98	+52:11:43.4	5BZQ J1740+5211	FSRQ	7C 173928.89+521311.00 (QSO)
G100.13+29.16	0.046	18:06:50.68	+69:49:28.1	5BZB J1806+6949	BL Lac	7C 180717.89+694858.00 (BLL)

Table 2 – *continued*

PCCS1 030	z	RA	Dec.	Name	Class	Comment
G085.73+26.11	0.663	18:24:07.07	+56:51:01.5	5BZB J1824+5651	BL Lac	7C 182315.19+564917.00 (BLL)
G077.23+23.50	0.695	18:29:31.80	+48:44:46.7	5BZU J1829+4844	Blazar Uncertain type	2C 1569 (Sy1)
G097.50+25.03	0.657	18:49:16.08	+67:05:41.7	5BZQ J1849+6705	FSRQ	ICRF J184916.0+670541 (Sy1)
G090.09–25.64	0.79	22:36:22.47	+28:28:57.4	5BZQ J2236+2828	FSRQ	QSO B2232+282 (BLL)
G086.10–38.18	0.859	22:53:57.75	+16:08:53.6	5BZQ J2253+1608	FSRQ	3C 454.3, [RKV2003] QSO J2253+1608 (QSO with absorption lines)
G108.97–09.47	1.279	23:22:26.00	+50:57:52.0	5BZQ J2322+5057	FSRQ	ICRF J232225.9+505751 (QSO)
G091.12–47.97	1.843	23:27:33.58	+09:40:09.5	5BZQ J2327+0940	FSRQ	QSO B2325+093

Notes. Redshifts are from BZCAT and references therein unless otherwise specified. The three resolved sources are excluded from the VLA sample. ^aSchmidt (1965). ^bTrager et al. (2000). ^cPopescu et al. (1996). ^dMeisner & Romani (2010). ^eHuchra, Vogeley & Geller (1999). ^fde Vaucouleurs et al. (1991).

Table 3. Dates on which the sources were observed. ‘Num.’ refers to the number of target sources observed in each observation. ‘Beam size’ is the average synthesized beam major and minor full width at half maximum, in arcsec.

Project code	Date	Num.	Flux calibrator	VLA config.	Beam size
15A-083	10/3/2015	19	3C 48	B	0.3×0.2
15A-083	15/3/2015	17	3C 48	B	0.4×0.2
16A-035	15/2/2016	18	3C 286	C	1.2×0.7
16A-035	11/3/2016	11	3C 48	C	1.3×0.7
17A-027	16/6/2017	8	3C 48	C	0.8×0.7
18B-003	18/11/2018	8	3C 286	C	0.9×0.7
18B-003	27/11/2018 ^a	5	3C 286	C	0.9×0.7
18B-003	14/12/2018	4	3C 286	C	1.0×0.7
18B-003	16/12/2018 ^b	5	3C 286	C	0.8×0.7
18B-003	28/1/2019	6	3C 286	C	1.4×0.7

^aData affected by instrumental issues and not used.

^bRepeat of 27/11/2018 observation.

We then follow EVLA Memo 201 (Hales 2017a,b) for the polarization calibration strategy, in particular following strategy ‘C1’ with one unpolarized calibrator and one calibrator with known polarization:

(i) Set the full polarization model for the flux density calibrator using fits to polarization fractions and angle as a function of frequency from Perley & Butler (2013). If using 3C 48, which is resolved, flag baselines where the model/flux is less than 90 per cent of the total model I flux and treat as an unresolved source.

(ii) Find cross-hand delay (‘KCROSS’) solutions using calibrator with known polarization.

(iii) Solve for polarization leakage per-channel (‘DF’) using the unpolarized calibrator if bright enough; otherwise (observations using J1407+2827 only) solve using a combination of the science targets (see below for more details).

(iv) Solve for the absolute polarization angle (‘XF’) using calibrator with known polarization.

As for the total intensity measurements, we solve for the spectral energy distributions of the sources in polarization in the uv -plane; this will be described in Section 3.2. We also check the image and uv -plane for significant residuals from the point-source model and find none with the exception of the source PCCS1 G182.17+34.17, which displays significant polarization residuals at the positions of the intensity peaks seen in Fig. A42. For consistency with the other sources, we quote the point-source fit for this source; however, clearly

when observed by a lower resolution instrument such as QUIJOTE, this source would appear to have a different polarization.

In the 2018–2019 observations, the polarization leakage calibrator J1407+2827 had become too faint to successfully solve for the per-channel leakage solutions. We therefore adapted our calibration procedure as follows. We made a first-pass leakage calibration with J1407+2827 using per-spectral-window (‘D’) solutions. We then used all science targets with polarization fractions < 5 per cent (from the first-pass analysis), plus 3C 286, to make a second-pass solution, as follows. We used the first-pass solution to insert a model for the polarized flux for all sources. We then repeated the polarization leakage calibration using ‘DF+X’ mode to solve simultaneously for the leakage and polarization angle terms. We expect any errors in the first-pass solution to leave only a small polarized residual that will tend to cancel out between the different sources since the polarization angles are uncorrelated. We then solve for the polarization angle using 3C 286 as usual.

To demonstrate the validity of this method, in Fig. 1 we show a comparison between some sources calibrated using this method and with the ‘D’ solutions using J1407+2827; it is clear that the results are the same but the calibration is more accurate. We also attempted a more standard calibration by merely substituting J1407+2827 with the source with the lowest polarization fraction, as determined using the J1407+2827 ‘D’ solutions. We show an example calibration of this type in Fig. 1 as well; although the new leakage calibration source has a very low polarization fraction of $p_{34} = 0.4$ per cent, it is still detected and using it as the leakage calibrator gives results that are biased with respect to the J1407+2827 and combined solutions. Our ‘combined’ method is therefore the best way to calibrate the polarization leakage given the limitations of the data. We apply this method also to the 2016 observation using J1407+2827 as the leakage calibrator to improve the SNR of the leakage solutions.

3.1 Calibration accuracy

The expected calibration accuracy is 5 per cent given that we are using the three-bit samplers and therefore cannot apply the switched power calibration.² Given the variable nature of the sources, assessment of the calibration accuracy requires simultaneous monitoring. We use two data sets for this purpose; the Metsähovi 37-GHz blazar monitoring data (Terasranta et al. 1992) and the Owens Valley Radio Observatory (OVRO) blazar monitoring data at 15 GHz (Richards et al. 2011); since many of our sources are frequently monitored by

²See <https://science.nrao.edu/facilities/vla/docs/manuals/oss/performance/vla-samplers#section-1> for an explanation of the expected calibration accuracy.

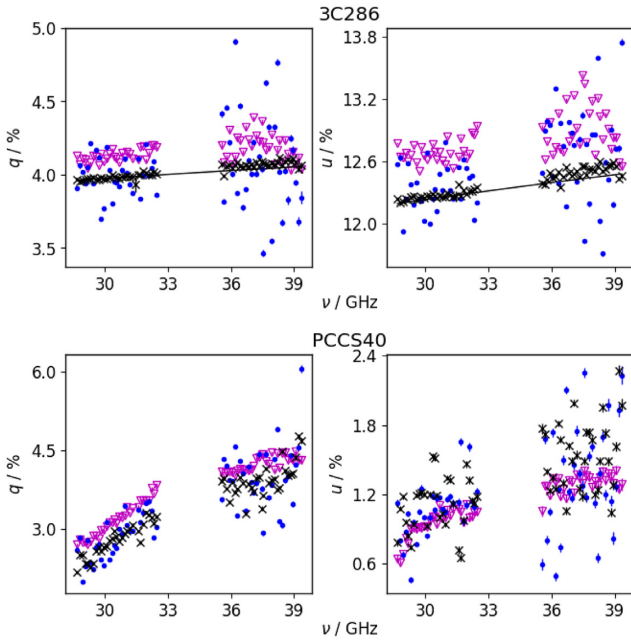


Figure 1. q and u values recovered in each spectral window for two sources in the 2018 December 14 observation, after full calibration using (i) ‘D’ solutions using J1407+2827 (blue dots); (ii) ‘DF+X’ solutions using all science targets with $p_{34} < 5$ per cent (black crosses); (iii) ‘DF’ solutions using PCCS1 G174.43+69.81 with a low $p_{34} = 0.4$ per cent (magenta triangles). In the 3C 286 plot, the black line is the model. The ‘DF+X’ solutions clearly lead to a more accurate calibration that is unbiased compared to the model and the (less accurate) J1407+2827 calibration; the PCCS1 G174.43+69.81 calibration is biased even though the polarization fraction is very small.

both programmes, we can interpolate the monitoring flux densities to the appropriate time and compare to our VLA measurements.

In the case of Metsähovi, we find 48 semi-simultaneous (within 10 d) measurements of 30 sources, including the calibration source 3C 84. We correct our VLA measurements to 37 GHz using the fitted in-band spectral index and compare the measured flux densities; this is shown in Fig. 2. In general, we see good agreement. There is a slight overabundance of sources with significantly low VLA flux density compared to Metsähovi, which probably indicates a resolution effect. The Metsähovi beam is 2.4 arcmin at 37 GHz. The VLA primary beam across our band has an FWHM of at most 1.6 arcmin, and the shortest VLA baselines are ≈ 10 k λ measuring structure on ~ 20 -arcsec scales, so both nearby sources outside of the VLA primary beam and flux resolved on scales between 20 arcsec and 2.4 arcmin would be included in the Metsähovi measurements but not detectable on our VLA maps. In addition, the Metsähovi error bars are relatively large (3 per cent systematic error for the brightest sources, and errors up to 20 per cent for the faintest in the overlapping sample), and the light curves are often sparsely sampled (around 20 day average cadence). The combination of resolution, large error bars, and sparse sampling makes testing for the expected ~ 5 per cent VLA calibration uncertainty difficult using the Metsähovi data. Fitting a straight line to S_{VLA} versus $S_{\text{Metsähovi}}$ using orthogonal least-squares regression gives a slope and offset consistent with 1 and 0 within 2σ , where σ are the error bars of the fit. We also note that the measurements of the brightest source, 3C 84, are consistent within 2σ (without adding additional calibration errors to the VLA data) and conclude that the VLA and Metsähovi data are consistent within the limitations of the data.

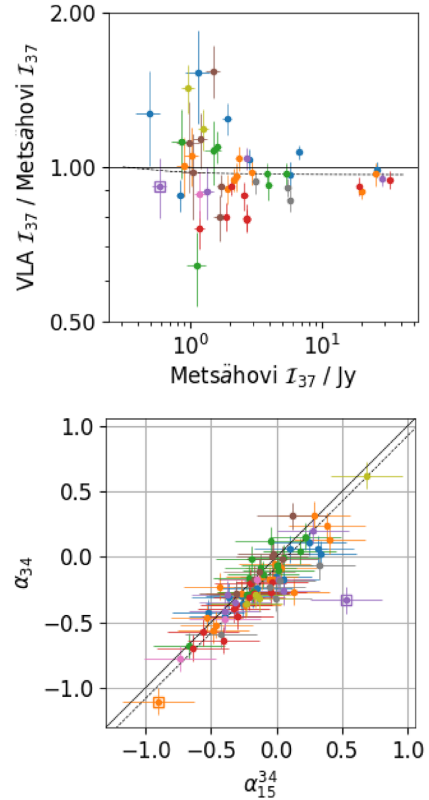


Figure 2. Simultaneous 37-GHz total intensity flux densities measured by Metsähovi and the VLA (top), and simultaneous 15–34 GHz spectral indices, α_{15}^{34} , calculated using the OVRO blazar monitoring data, compared to spectral indices across the VLA bands, α_{34} (bottom). The points are coloured by VLA observing epoch. In both cases, the solid black line shows a one-to-one correspondence while the black dashed line shows the best straight-line fit using orthogonal least-squares regression. In the Metsähovi plot, no extra systematic errors have been added to the VLA data-points. In the OVRO plot, conservative VLA calibration uncertainties of 5 per cent in the reference flux density and 0.1 in the spectral index are included in the error bars plotted and used for the least-squares fit. The points marked with squares in both plots are PCCS1 G107.00–50.62, which may have a turnover in its spectrum considering the 37-GHz flux agrees well but the spectral index is discrepant with OVRO. These points are excluded from the fit to the OVRO data.

In the case of OVRO, we find 83 semi-simultaneous measurements of 43 sources. To compare the VLA and OVRO flux measurements, we calculate spectral indices between 15 and 34 GHz. Assuming that there is no spectral curvature between 15 and 40 GHz, this should be equal to the spectral index over the VLA bands. Fig. 2 shows that there is indeed a very good correspondence between these quantities. We assume offsets from this relationship will be dominated by the VLA systematic calibration uncertainties in α_{34} due to the much shorter frequency lever arm and therefore use this comparison to test for the value of this uncertainty. We do this by fitting a straight line to the data (excluding the significant outlier PCCS1 G107.00–50.62) using orthogonal least-squares regression. We use the OVRO errors as given in the data base and use error propagation to calculate the error in the interpolated quantity. We add an extra VLA calibration error in α_{34} to the statistical error calculated from the fit over the VLA band, and increase this error until reduced $\chi^2 = 1$ for the linear fit. This gives a spectral index calibration error of 0.1, which will be a conservative estimate, given that we have not included any VLA systematic flux density calibration errors. The orthogonal

least-squares regression, with the nominal 5 per cent flux density calibration uncertainty and spectral index calibration uncertainty of 0.1 added to the statistical errors in quadrature, gives a best-fitting slope consistent with one (1.00 ± 0.06) and some indication of an offset (-0.08 ± 0.02). This may indicate a small systematic offset in the spectral indices fit across the VLA band; the effect of some sources having flux resolved out as described above for the Metsähovi comparison; or a true slight steepening on average of the spectral indices from 15 to 40 GHz. We note that Sajina et al. (2011) found a steepening of spectral indices between 20 and 90 GHz and Planck Collaboration XLV (2016) found broken power-law fits were necessary between 1.1 and 857 GHz with the high-frequency spectral index typically steeper than the low-frequency spectral index. Given these uncertainties, we choose not to attempt to correct for this offset. We adopt the 5 per cent and 0.1 as the VLA systematic errors in central flux density and spectral index in the following variability analysis and add them in quadrature to the errors estimated from the fit to the VLA spectra; these are conservative upper limits to the true calibration accuracy as shown by the clearly overestimated total error bars in Fig. 2. We note that the two notable outliers (marked with squares in Fig. 2) are two measurements of the same source, PCCS1 G107.00–50.62. The single coincident VLA and 37 GHz Metsähovi measurement of this source agrees well, and it shows no non-core flux in the VLA maps (see Fig. A1), so it may instead have a turnover in its spectrum accounting for the discrepancy.

To estimate the systematic uncertainties in the polarized quantities, we follow Hales (2017b). For our ‘unpolarized’ calibrators used for leakage calibration, we estimate the uncertainty in the polarization fraction p_ϵ as the spurious on-axis fractional polarization produced by a small amount of polarization actually being present:

$$2(\sigma_d)^2 \approx p_{\text{true}}^2 + \frac{N_a}{A^2}$$

$$p_\epsilon \approx \sigma_d \sqrt{\frac{\pi}{2N_a}} \quad (1)$$

(using equations 30 and 28 from Hales 2017b), where σ_d is the error in the leakage ‘d-term’ calibration accuracy, N_a is the number of antennas, and A is the full-array dual-polarization total intensity S/N of the calibrator within the single spectral channel of interest. 3C 84 is known to approach 1 per cent true polarization at 43 GHz (e.g. <http://www.aoc.nrao.edu/~smyers/calibration/master.shtml>); J1407+2827 has been shown to have polarization of $\lesssim 0.3$ per cent at Q band (Liu et al. 2018) and < 0.2 per cent at K band (Oriente & Dallacasa 2008). We adopt $p_{\text{true}} = 1$ per cent for 3C 84 and 0.3 per cent for J1407+2827; in the case of the 2018–2019 solutions we conservatively adopt $p_{\text{true}} = 1$ per cent as the maximum residual with respect to the first-pass fit. This gives per-channel p_ϵ values < 0.2 per cent for 3C 84, between 0.5 and 3 per cent for J1407+2827, and between 0.2 and 0.3 per cent for the combined science targets, where the higher values are at the upper end of the frequency band where the S/N of most sources decreases.

Also following Hales (2017b), we estimate the error in the polarization angle estimates, Φ_ϵ , using their publicly available software POLCALSIMS³ (Hales 2017c) that uses Monte Carlo simulations to predict position angle error as a function of S/N of the polarized calibrator. The per-channel estimates range from 0:15 to 1:8 in the case of 3C 48 and 0:05 to 0:8 in the case of 3C 286, again with the higher errors corresponding to higher frequencies where the S/N of the sources is lower.

³<https://github.com/chrisshales/polcalsims>.

We assume both of these systematic errors are completely correlated between channels in a spectral window and so use the average per-channel estimate in each spectral window as the overall systematic error for the spectral window estimate. We use error propagation to translate these systematic errors in p and Φ in errors in q and u :

$$\Delta q_{\text{sys}}^2 = p_\epsilon^2 \cos^2(2\Phi) + 4u^2 \Phi_\epsilon^2$$

$$\Delta u_{\text{sys}}^2 = p_\epsilon^2 \sin^2(2\Phi) + 4q^2 \Phi_\epsilon^2. \quad (2)$$

3.2 qu -fitting

To fit the polarization properties, we take a vector average over time and baseline of the calibrated RL and LR cross-hand visibility data in each spectral window and solve for \mathcal{Q} and \mathcal{U} using

$$V_{RL} = \mathcal{Q} + i\mathcal{U}$$

$$V_{LR} = \mathcal{Q} - i\mathcal{U}. \quad (3)$$

We estimate the uncertainty in q and u using the standard deviation in the data and adding in quadrature the systematic errors estimated as in Section 3.1 (the error in \mathcal{I} is negligible compared to the error in \mathcal{Q} and \mathcal{U}).

We follow a similar qu -fitting procedure to O’Sullivan et al. (2012) in that we fit jointly to q and u , minimizing the total χ^2 (rather than fitting to p and Φ separately). This guarantees consistency between the derived p and Φ properties. Our frequency band does not contain enough information to usefully constrain physical parameters, so unlike O’Sullivan et al. (2012), rather than fitting a physical model we simply fit a power law to the polarization fraction as a function of frequency, and a rotation measure (RM) law, $\Phi = \Phi_0 + \text{RM}\lambda^2$ law to the polarization angle as a function of wavelength. This gives

$$q = p \cos(2\Phi) = p_0 \left(\frac{\nu}{\nu_0}\right)^{\alpha_p} \cos[2(\Phi_0 + \text{RM}\lambda^2)]$$

$$u = p \sin(2\Phi) = p_0 \left(\frac{\nu}{\nu_0}\right)^{\alpha_p} \sin[2(\Phi_0 + \text{RM}\lambda^2)], \quad (4)$$

where our reference frequency ν_0 is again 34 GHz. We use the SCIPY.OPTIMIZE.LEASTSQ least-squares fitting algorithm to find the best-fitting p_0 , α_p , Φ_0 , and RM and estimate their associated errors (Δp_0 , $\Delta \alpha_p$, $\Delta \Phi_0$ and ΔRM).

We have added the systematic errors to the per-spectral window q and u error estimates before performing the fits to account for small differences in systematic error levels across the frequency band. However, in general, we expect the errors to be correlated across the frequency band and therefore the parameter error estimates (produced assuming uncorrelated errors) will be underestimated. To account for this, we re-scale the q and u errors so that reduced $\chi^2 = 1$ for the fit and re-estimate the parameter errors; then we add in quadrature the mean p_ϵ (to Δp_0) and Φ_ϵ (to $\Delta \Phi_0$) to produce the final error.

The qu -fitting procedure using our simple model provides reasonable fits in all cases and we do not see systematic trends indicating a more sophisticated model would be warranted; some sample fits are shown in Fig. 3. We define as undetected in polarization those sources with fitted $p_0/\Delta p_0 < 3$. We note that there are no $n\pi$ ambiguities in the fitted RMs, since our frequency channels are closely spaced. We note also that this method circumvents the issue of bias in polarization fraction (i.e. $p_{\text{meas}} = \sqrt{(q + \sigma_q)^2 + (u + \sigma_u)^2} > p_{\text{true}} = \sqrt{q^2 + u^2}$) since we are fitting a spectrum in q and u across a large number of frequency measurements, each of which can be displaced in either the positive or negative direction. This is demonstrated in Fig. 4 where we show the fit to J1407+2807,

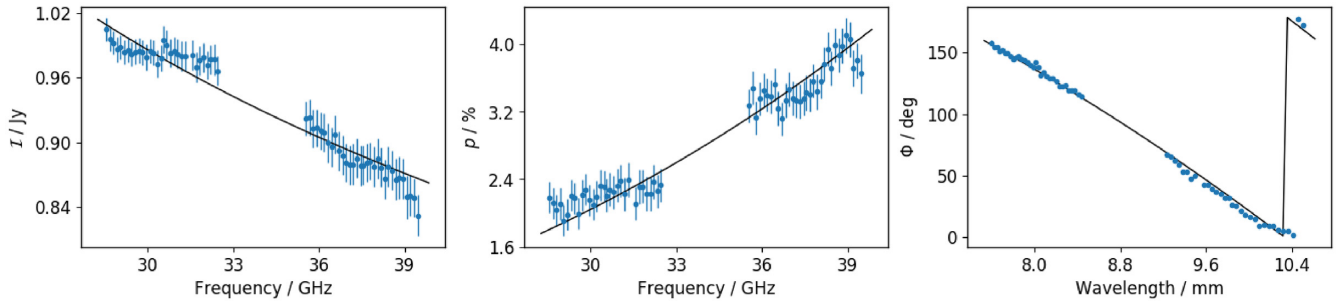


Figure 3. Sample fits to the uv -plane flux densities: The left-hand panel shows total intensity, centre polarization fraction, and right polarization angle as a function of frequency. The source is PCCS1 G147.84-44.04, observed on 2015 October 3, which shows the most extreme RM in the sample. In all cases, each point represents a spectral window. In the total intensity plot, the error bars are derived from the scatter within the frequency channels in the spectral window. In the polarization plots, the error bars represent the scatter within the frequency channels added in quadrature with the systematic errors estimated as described in Section 3.1. The error bars do not take into account correlations between frequency channels and/or baselines and are not independent.

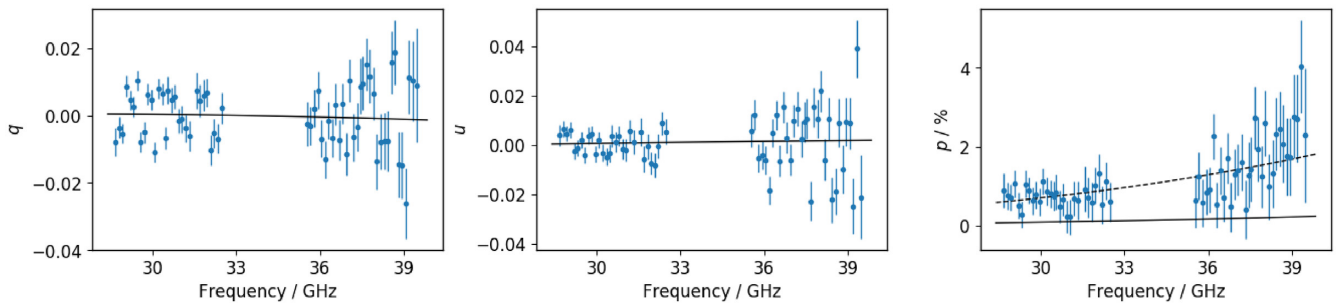


Figure 4. Sample fits to the polarization spectrum of J1407+2827, a low-SNR source with negligible polarization. From the left- to right-hand side, we show q , u , and p . As in Fig. 3, the error bars are the total error including statistical and systematic contributions. The solid black lines show fits to the data-points using the qu -fitting method, while the dashed black line in the p plot shows the bias that would result from fitting directly to $p = \sqrt{q^2 + u^2}$.

the low-SNR source with negligible polarization. The qu -fitting method clearly produces an unbiased result whereas fitting directly to $p = \sqrt{q^2 + u^2}$ produces a biased result.

4 RESULTS

In Table 4, we show a sample section of our results table, containing flux density and spectral index estimates in total intensity and polarization fraction, as well as polarization angles extrapolated to $\lambda = 0$ and RM estimates.

4.1 Total intensity properties

In Fig. 5, we show the distributions of central flux densities (at 34 GHz) and spectral indices, including each epoch of measurement for each source separately. These show that most (87 per cent) of the sources are flat-spectrum with fitted spectral indices $\alpha > -0.5$. This is as expected given the high-frequency selection criterion and in agreement with the BZCAT classifications. We also see that although the sources were selected to be brighter than 1 Jy at 30 GHz, in fact, only slightly more than half (61 per cent) have 34 GHz flux densities greater than 1 Jy; this shows the variability of these sources and highlights the difficulty in selecting a complete sample.

4.1.1 Total intensity variability

Since we only have two epochs of observation for each source, we first use the Metsähovi light curves to check whether our observations can fairly test the variability of our sample. For each of the 31

(out of 54) sources with Metsähovi measurements spanning ≈ 4 yr, we produce a histogram of the ‘true’ variability by stacking all the measurements of $(\mathcal{I} - \bar{\mathcal{I}})/\bar{\mathcal{I}}$, where \mathcal{I} are the individual flux measurements and $\bar{\mathcal{I}}$ is the mean flux density for each source over the whole light curve. Then, we replicate our VLA sampling by interpolating the light curves at points corresponding to the VLA measurements for each source, which produces 55 individual measurements. We calculate the fractional variation for these points as above, with respect to the mean over the whole light curve. Fig. 6 shows the resulting two histograms. They are of course not identical but show very similar distributions, and the standard deviation of each set of measurements is nearly identical, $\sigma = 0.30$ and 0.29 . Restricting the sample to sources for which we have two VLA measurements (24 sources) does not change the distribution or the standard deviation. We therefore can be confident that, although we only have two epochs of measurement, our sample of sources is large enough to ensure that we are probing the variability statistics of the overall sample fairly. We note that there is a small asymmetry to larger positive values of the fractional variation apparent in both histograms, which can be explained by the fact that most sources spend a large fraction of their time near a ‘baseline’ flux density value, with occasional excursions to very high, flaring states. This results in the mean over a long period of time being closer to the baseline, and the flares appearing as large, positive fractional deviations.

Now considering the VLA measurements, in Fig. 7, we show histograms of the variability in total intensity flux density and spectral index for the 41 sources for which we have two measurements. Since we only have two measurements of each source, we define fractional variation in flux density as $(\mathcal{I}_{34,2} - \mathcal{I}_{34,1})/\bar{\mathcal{I}}_{34}$, where $\bar{\mathcal{I}}_{34}$

Table 4. A sample section of the results table.

PCCS1 030	Epoch (MJD)	I_0 (Jy)	ΔI_0 (Jy)	α	$\Delta\alpha$	p_0	Δp_0	α_p	$\Delta\alpha_p$	Φ_0 (°)	$\Delta\Phi_0$ (°)	RM (rad m ⁻²)	Δ RM (rad m ⁻²)
G178.26+33.40	57091.06	0.6300	0.0315	-0.360	0.101	0.029 72	0.001 86	0.080	0.073	108.32	1.18	391	223
G182.17+34.17	57091.06	0.7121	0.0356	-0.426	0.101	0.061 89	0.001 91	0.323	0.079	44.50	0.68	-789	93
G200.04+31.88	57091.06	0.7326	0.0366	0.058	0.101	0.016 24	0.001 95	-0.358	0.360	31.72	1.70	3003	330
G143.53+34.42	57091.06	2.8432	0.1422	0.171	0.101	0.018 85	0.001 33	-1.187	0.139	92.04	0.86	961	162
G206.82+35.81	57091.06	5.5528	0.2777	-0.156	0.101	0.020 64	0.001 86	0.551	0.101	144.15	0.93	160	169
G175.72+44.81	57091.06	2.3493	0.1175	0.022	0.100	0.019 57	0.001 86	-0.793	0.105	76.35	1.53	-1007	301
G152.23+41.00	57091.06	0.8449	0.0423	-0.245	0.101	0.040 56	0.001 92	0.226	0.122	137.42	0.87	-1529	150
G198.82+44.43	57091.06	0.9126	0.0456	0.238	0.100	<0.005 58	0.001 86	-	-	-	-	-	-
G183.71+46.17	57091.06	7.3728	0.3687	-0.301	0.101	0.017 72	0.002 04	0.096	0.460	137.41	1.35	-195	240
G181.02+50.29	57091.06	0.5709	0.0286	-0.455	0.100	0.014 40	0.001 85	-0.899	0.114	176.76	1.53	4664	300

Notes. Each source has a separate entry for each epoch showing flux density at the central frequency of 34 GHz and spectral index in total intensity; polarization fraction (not per cent) at 34 GHz and spectral index, extrapolated polarization position angle and RM, along with associated errors. The errors in the table include the systematic errors estimated as in Section 3.1. The full table is available as an online-only supplement and at CDS.

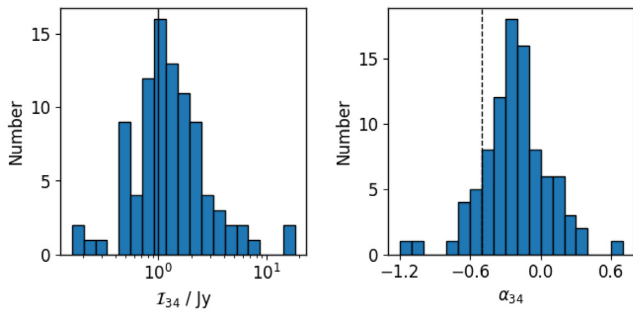


Figure 5. Distributions of total intensity flux densities at 34 GHz (left-hand panel) and spectral indices (right-hand panel) across the VLA observation band. The solid line in the flux density histogram indicates the selection cut at 1 Jy (at 30 GHz, but we do not correct for the small frequency shift) and the dashed line in the spectral index histogram indicates the traditional division into steep- and flat-spectrum sources.

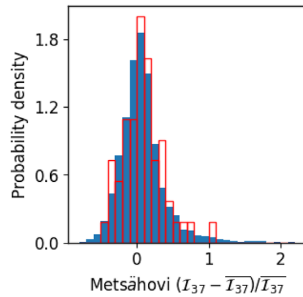


Figure 6. Stacked distributions of fractional variations in \mathcal{I} with respect to the mean for sources with Metsähovi light curves. The blue, filled histogram shows the total light curve while the red, unfilled histogram shows the distribution when sampling each light curve only at two points, mimicking the VLA sampling.

is the weighted mean of the two flux densities, and spectral index variation as $\alpha_2 - \alpha_1$. We attempt to quantify the variability as follows. We have no reason to expect the flux and spectral index to change more in one direction than the other, given that the sources were observed at different epochs and all will have different variability time-scales; we do not expect to see the bias toward positive fractional deviations in \mathcal{I} found in the Metsähovi measurements above since our fractional deviations are with respect to the weighted mean of two measurements only, rather than the whole light curve. Therefore,

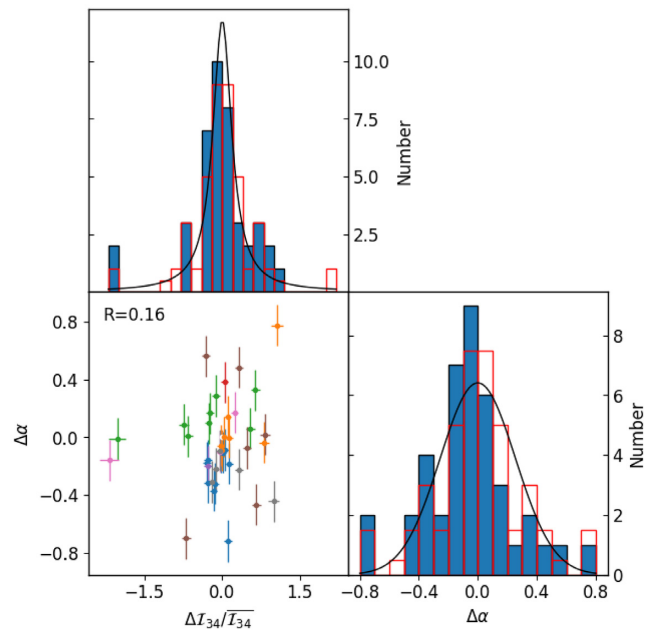


Figure 7. Histograms of fractional variation in total intensity flux density and spectral index variation (histograms), and correlation between these quantities colour-coded by epoch pair. Along with the histograms of the data (solid blue), we also plot the ‘symmetrized’ histograms (red outlines; normalized by a factor of 2 for comparison with the non-symmetrized histograms) as described in the text. The black lines show Cauchy (Gaussian) fits to the symmetrized flux density (spectral index) variation distributions; see text for more details.

we symmetrize the distributions by adding the reflection of each point to the data set, i.e. our symmetrized data sets consist of $[(\mathcal{I}_{34,2} - \mathcal{I}_{34,1})/\overline{\mathcal{I}}_{34}, (\mathcal{I}_{34,1} - \mathcal{I}_{34,2})/\overline{\mathcal{I}}_{34}]$ and $[\alpha_2 - \alpha_1, \alpha_1 - \alpha_2]$.

To fit a model probability distribution to each of the variability distributions, we use a Kolmogorov–Smirnov (KS) test. For a given model for the distribution (either Cauchy or Gaussian) and appropriate set of parameters for the model, we calculate the KS ‘D’-statistic between the symmetrized data and the model that gives a measure of the maximum difference between the cumulative probability distributions of the two. We then vary the parameters in the model until the smallest ‘D’-statistic is reached, i.e. finding the set of parameters that best match that model to the data. This

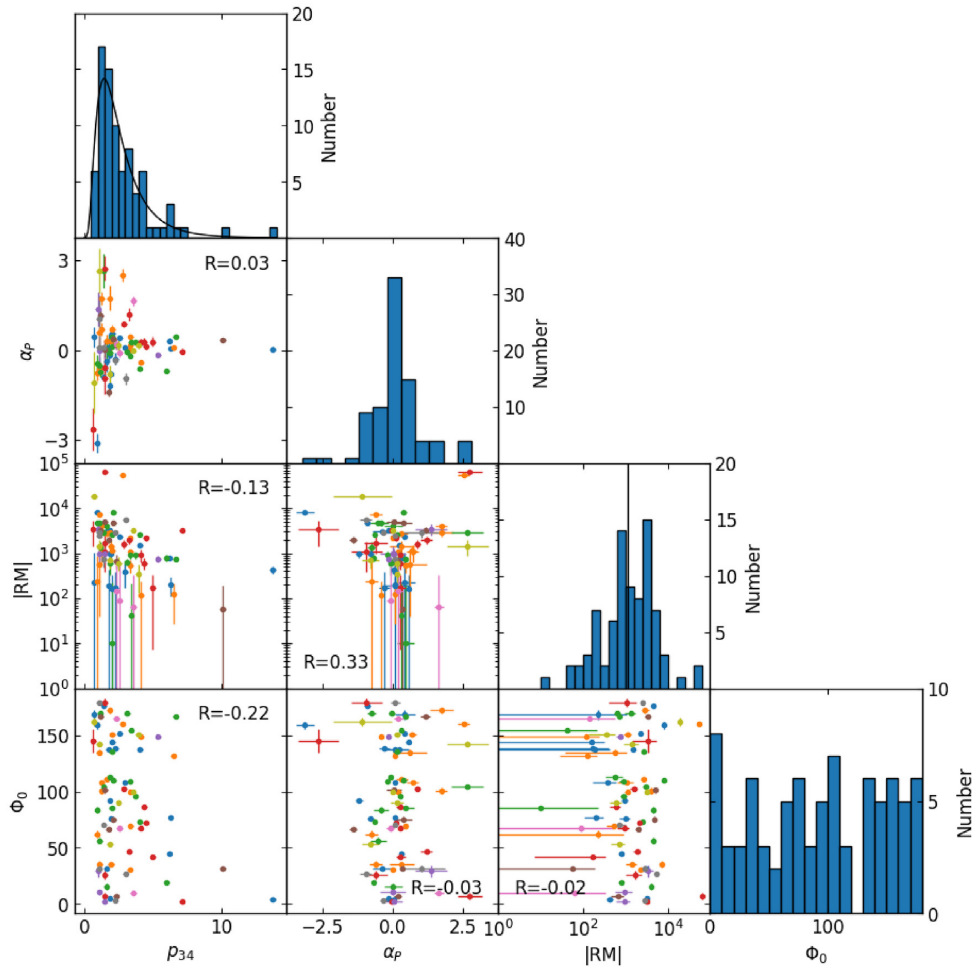


Figure 8. Histograms showing the distribution of polarization fractions (in per cent), polarization spectral indices, RM (in rad m^{-2}) and intrinsic polarization angles (in degrees) fit across the VLA bands, and correlations between the four quantities. The histogram of polarization fractions also shows a lognormal fit to the distribution and the median RM is indicated with a vertical line on the histogram. Points are colour-coded by observing epoch as in Fig. 2.

method has the advantage that the fit to the model does not depend on how the data are binned.

In the case of the flux density variations, we find a Cauchy distribution centred at 0 fits the distribution well, i.e.

$$\text{PDF} \left(\frac{\Delta I_{34}}{\mathcal{I}_{34}} \right) = \left\{ \pi \gamma \left[1 + \left(\frac{\Delta I_{34}}{\mathcal{I}_{34} \gamma} \right)^2 \right] \right\}^{-1}, \quad (5)$$

with the best-fitting $\gamma = 0.22$. The KS test ‘D’-statistic between the symmetrized (non-symmetrized) data and the fitted Cauchy distribution is 0.04 (0.08) and the p -value is 1.00 (0.96), indicating a good fit even to the non-symmetrized data. We show both the symmetrized and non-symmetrized data in Fig. 7, along with the best-fitting Cauchy distribution.

In the case of the α variation, we find a Gaussian distribution to be a better fit than a Cauchy distribution, although clearly it does not fit the data particularly well. We find a best-fitting standard deviation $\sigma = 0.26$ with mean μ fixed to 0. The KS test ‘D’ values between the symmetrized (non-symmetrized) data and the fitted distribution are 0.04 (0.18) and the p -values are 1.00 (0.13). The measurements are clearly limited by the relatively large spectral index calibration error, and more accurate measurements with a longer frequency lever arm would be required to investigate further the spectral index variability.

Fig. 7 also shows the correlation between variability in (non-symmetrized) total intensity flux density and spectral index, which is weak with Pearson $R = 0.16$, p -value=0.33, indicating that there is not enough information in our two-point estimates to investigate the physical mechanisms underlying the changes. In general one would expect a change in flux density to be accompanied by a change in spectral index and vice versa. There are, however, some cases where a highly significant variation in spectral index occurs although the flux density is nearly constant; we investigate one of these cases in Section 5.1. A change in spectral index is therefore also a good indicator of variability. In total, 59 per cent of the sources have a change in either flux density or spectral index of $>3\sigma$ (using the systematic errors as calibrated in Section 3.1).

4.2 Polarization properties

We detect 85 per cent of the sources in polarization, considering all observing epochs together. In Fig. 8, we show the distributions of polarization fractions, spectral indices, RM and intrinsic polarization angles fit to the polarization fraction spectra as well as correlations between the four quantities. We see fairly low polarizations in most cases, with a median of 2.2 per cent; this is consistent with other studies at similar frequencies (e.g. Battye et al. 2011; Sajina et al.

2011) and indicates that we are seeing mostly the flat-spectrum core rather than the steep-spectrum lobes, which are more highly polarized. We also show a lognormal fit to the distribution, made by minimizing the KS ‘D’-statistic between the data and a lognormal distribution. This gives fitted parameters $(\mu, \sigma) = (2.20, 0.64)$ that are in good agreement with the fits to flat-spectrum source data at various frequencies from Puglisi et al. (2018) (e.g. their fig. 3). We see a fairly broad distribution of spectral indices in polarization (although these do have large errors due to the small change observed over the band), with ≈ 26 per cent of sources having rising spectra at $>3\sigma$ significance indicating depolarization, and ≈ 15 per cent having falling spectra at $>3\sigma$ significance indicating repolarization (we note that repolarization can occur as a consequence of physical models more complicated than a single Faraday screen; see e.g. O’Sullivan et al. (2012) for example models and data). We do not attempt fits to the α_p and $|RM|$ distributions due to the large and non-uniform errors. As expected, the intrinsic polarization angles are uniformly distributed.

We note that the RMs in Fig. 8 are observed RMs with no correction for Galactic RM or conversion to the AGN rest frame since we are interested in the observed properties in the context of the QUIJOTE analysis. We detect an RM at $>3\sigma$ significance in 65 per cent of the polarization detections and find a median $|RM| \approx 1100 \text{ rad m}^{-2}$. Previous VLBI studies have found similarly high AGN core RMs at centimetre wavelengths (e.g. Zavala & Taylor (2004) find core RMs up to ≈ 2000 with mean of 644 rad m^{-2} between 8 and 15 GHz; Hovatta et al. (2012) find core RMs up to ≈ 1500 with a tail out to >6000 and median of 171 rad m^{-2} between 8 and 15 GHz) while the jet RMs tend to be lower. This lends additional support to the idea that our 30–40 GHz observations are mostly probing the core. Hovatta et al. (2019) find that RM increases as a function of frequency in 3C 273 with $RM \propto \nu^2$ in agreement with models for a sheath surrounding a conically expanding flow; if this effect occurs for the majority of sources it would explain our somewhat higher median. Indeed, Algaba et al. (2011) find a median RM of $\approx 1600 \text{ rad m}^{-2}$ between 15 and 43 GHz, although their values may suffer from $n\pi$ ambiguities. We see one extreme outlier in RM that we describe in more detail in Section 5.2.

The only significant correlation between the polarization properties is between the α_p and $|RM|$ measurements, with Pearson $R = 0.33$, p -value = 0.002. This is as expected since a higher RM should imply a greater degree of depolarization at lower frequency, and therefore large, positive α_p . However, the sources with significantly negative α_p also seem to show a high RM, suggesting the situation is more complicated than a single Faraday screen and the polarization angle spectra just happen to follow a λ^2 law over the relatively small range in wavelength. Given the uncertainties introduced by averaging over our relatively large beam (compared to VLBI studies that resolve the source structure), we do not investigate this further.

4.2.1 Polarization variability

In Fig. 9, we show the distributions of and correlations between the variation in polarization fraction, spectral index, RM, and intrinsic polarization angle for the sample. There are 34 sources with more than one detection; of these 65 per cent are variable in p_0 and all are variable in one or more of these quantities at 3σ (where σ includes systematic and statistical contributions as described in Section 3.2). The notable outlier in polarization fraction is PCCS1 G145.78+43.13 that we investigate further in Section 5.3. Aside from this extreme outlier, the distribution of changes in polarization fraction is relatively Gaussian; a fit to the symmetrized

data excluding the outlier gives a best-fitting $\sigma = 1.8$ per cent. The KS test comparing the symmetrized (non-symmetrized) data to a normal distribution centred at 0 with this standard deviation gives a p -value of 1.00 (0.96), indicating good agreement.

The changes in polarization fraction spectral index and RM are clustered around 0, with the exception of PCCS1 G145.78+43.13. It is more difficult to assess the Gaussianity of these distributions given the large variations in measurement errors. Most of the outliers do have large errors. Of the two highly significant outliers, one is PCCS1 G145.78+43.13, as already mentioned and OVRO monitoring of the second, PCCS1 G129.09-13.46 shows that the two observations similarly took place during a quiescent period and a flare so these large changes are likely genuine.

We see a significant correlation between $\Delta\alpha_p$ and $\Delta|RM|$ with Pearson $R = -0.42$ and p -value=0.01. This is in line with the correlation between α_p and $|RM|$ discussed in Section 4.2; a source undergoing a higher degree of depolarization has a higher RM. Removing PCCS1 G145.78+43.13 strengthens the correlation slightly to $R = -0.46$, p -value = 0.006. We also see a highly significant correlation between Δp_{34} and $\Delta|RM|$ with $R = -0.67$, p -value = 1×10^{-5} ; however, this correlation is largely driven by PCCS1 G145.78+43.13 and removing this outlier decreases the correlation strength to $R = -0.27$, p -value=0.13. This correlation is also consistent with the idea that a higher RM implies a higher degree of depolarization, so increase in RM correlates with decrease in polarization fraction.

4.3 Correlations between total intensity and polarization

In Fig. 10, we show the correlation between total intensity parameters and polarization parameters. All appear uncorrelated. Of particular importance for predicting the contamination to B-mode analysis is the correlation between total intensity flux density and polarization fraction; i.e. if simulating point source contamination, can random values be drawn independently from the total intensity source count and polarization fraction distribution, or is there a correlation? Although the Pearson R value for p_{34} versus \mathcal{I}_{34} is low ($R = -0.04$, $p = 0.70$), a correlation could be obscured by the distribution of \mathcal{I} values. We test this idea by dividing the sources into three bins in \mathcal{I} and calculating median polarization fractions in each bin. We see a slight positive correlation between flux density and median polarization fraction. To test the statistical significance of the trend, we calculate KS test statistics between the polarization fractions in each bin and the overall fitted lognormal distribution. The results for the bins are summarized in Table 5; we find that for the lower and middle flux density bins, the p -values are ≈ 0.06 and 0.2, respectively, indicating that similar data could be drawn from the overall distribution only ≈ 6 and 20 per cent of the time. This is contrary to the lack of correlation found by Battye et al. (2011) and Massardi et al. (2008), although we emphasize that the sample size is small and there could be a selection effect given that our sources were selected to be brighter than 1 Jy (i.e. sources in the lower flux density bin must be very variable and currently in a relatively quiescent state). The effect is sensitive to the boundary of the lower bin and disappears if, for example, the boundary is placed at 1.0 Jy rather than 0.6 Jy. A sample complete to a lower flux density limit would be required to investigate this further.

We also test the correlation between total intensity spectral index and polarization fraction. Here we see no evidence for correlation ($R = -0.02$, $p = 0.85$) and no evidence for a different distribution of polarization fractions when we divide into two bins at $\alpha_{34} = -0.5$. The medians and p -values are also reported in Table 5.

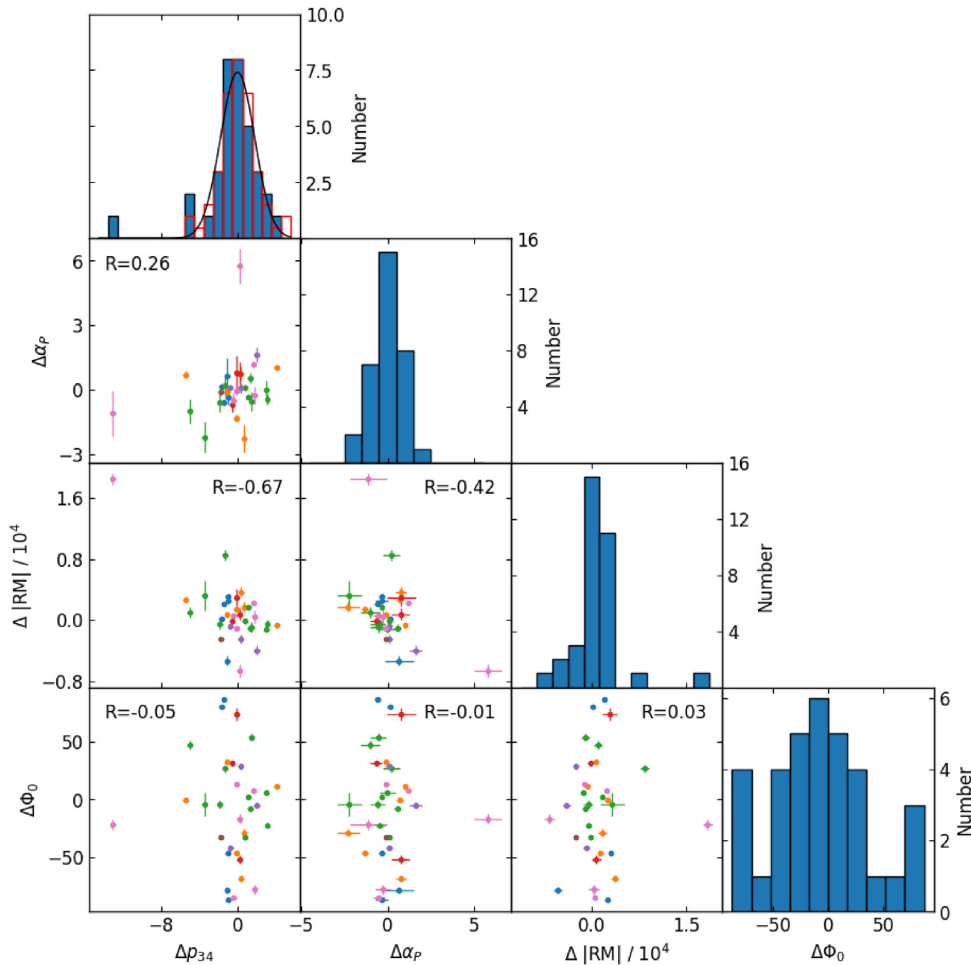


Figure 9. Histograms showing the distribution of variation in polarization fraction (in per cent), polarization spectral index, RM (in rad m^{-2}) and intrinsic polarization angle (in degrees) fit across the VLA bands, and correlations between the four quantities. Points are colour-coded by observing epoch pair as in Fig. 7. The histogram of polarization fraction (in per cent) also shows a normal distribution centred at 0 with standard deviation equal to the standard deviation measured from the observed distribution, excluding the large outlier.

In Fig. 11, we show correlations between the variations in total intensity flux density and spectral index with variation of the polarization parameters. Here too we see very little correlation, as evidenced by the very low Pearson R -coefficients shown on the plots. There seems to be a slight correlation between $\Delta\alpha$ and $\Delta\alpha_P$ ($R = -0.19$; $p = 0.09$), which may indicate that sources coming down from a flare (becoming more optically thin) are also becoming less depolarized (α_P becoming less positive), and vice versa.

5 RESULTS FOR SOME INDIVIDUAL SOURCES

Here we investigate in more detail some of the interesting results for individual sources.

5.1 PCCS1 G156.86–39.13

PCCS1 G156.86–39.13 is one of the cases where $\Delta\alpha$ is large yet its flux density is nearly constant. It has coverage from OVRO and also at 43 GHz from the VLBA-BU Blazar Monitoring Project.⁴ Its light curve is shown in Fig. 12. The VLA data-points are consistently

⁴<http://www.bu.edu/blazars/VLBAproject.html>.

above the VLBA light curve since the VLBA resolves out some of the flux from the source; however, we can see that the two VLA epochs of observing happen to catch the source on either side of a peak so that the flux density is approximately the same. Comparing the OVRO and VLBA light curves, we can see that the 43 GHz flux density decreases more quickly than the 15-GHz flux density for both this peak and the earlier peak, indicating a change in optical depth. This is consistent with the VLA spectral indices changing from slightly positive (optically thick) to slightly negative (optically thin) between the two epochs.

5.2 PCCS1 G147.84–44.04

PCCS1 G147.84–44.04 or 4C 15.05 is an extreme outlier in RM, having $\text{RM} \approx -56\,000$ and $-64\,000 \text{ rad m}^{-2}$ in the two observation epochs; the polarization fits for the first epoch are shown in Fig. 3. At the redshift $z = 0.833$ of the source our observed frequency $\nu_{\text{obs}} = 34 \text{ GHz}$ corresponds to an emitted frequency $\nu_{\text{em}} = (1 + z)\nu_{\text{obs}} = 62 \text{ GHz}$ and the observed RMs correspond to an intrinsic RM of $(1 + z)^2 \text{RM}_{\text{obs}} \approx 2 \times 10^5 \text{ rad m}^{-2}$ in the source rest frame. To our knowledge, this source has not been identified as having a particularly high RM in any other work. Zavala & Taylor (2004) and Hovatta et al. (2012) both fail to measure RMs for this source

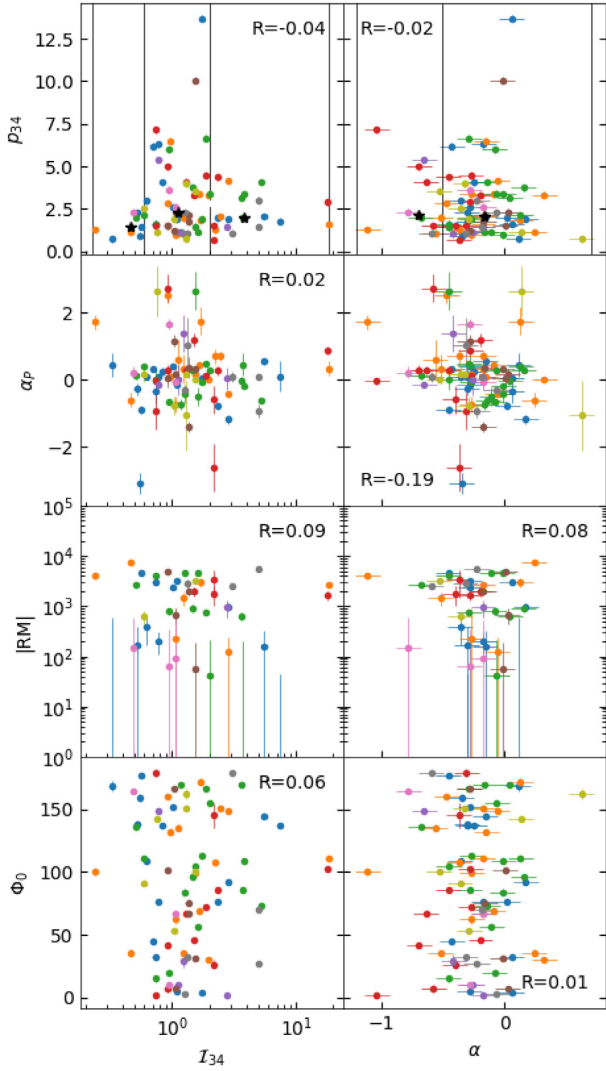


Figure 10. Correlations between total intensity flux density (left-hand column) and spectral index (right-hand column) with polarization parameters. In the p_{34} plots, the vertical lines show a division into flux density/spectral index bins, and the black stars show the median polarization fraction within the bins.

Table 5. Median polarization fraction (in per cent) and KS test p -values for polarization per centages in different bins in total intensity flux density (top) and spectral index (bottom), compared to the lognormal fit for the overall distribution.

\mathcal{I}_{\min}	\mathcal{I}_{\max}	n	p_{median}	$p\text{-value}$
0.23	18.4	82	2.06	0.95
0.23	0.60	9	1.44	0.060
0.60	2.0	52	2.29	0.25
2.0	18.4	21	2.03	0.59
α_{\min}	α_{\max}	n	p_{median}	$p\text{-value}$
-1.2	0.7	82	2.06	0.95
-1.2	-0.5	12	2.17	0.80
-0.5	0.7	70	2.06	0.94

Notes. Flux densities are in Jy and n is the number of sources in the bin. The top row is the overall distribution.

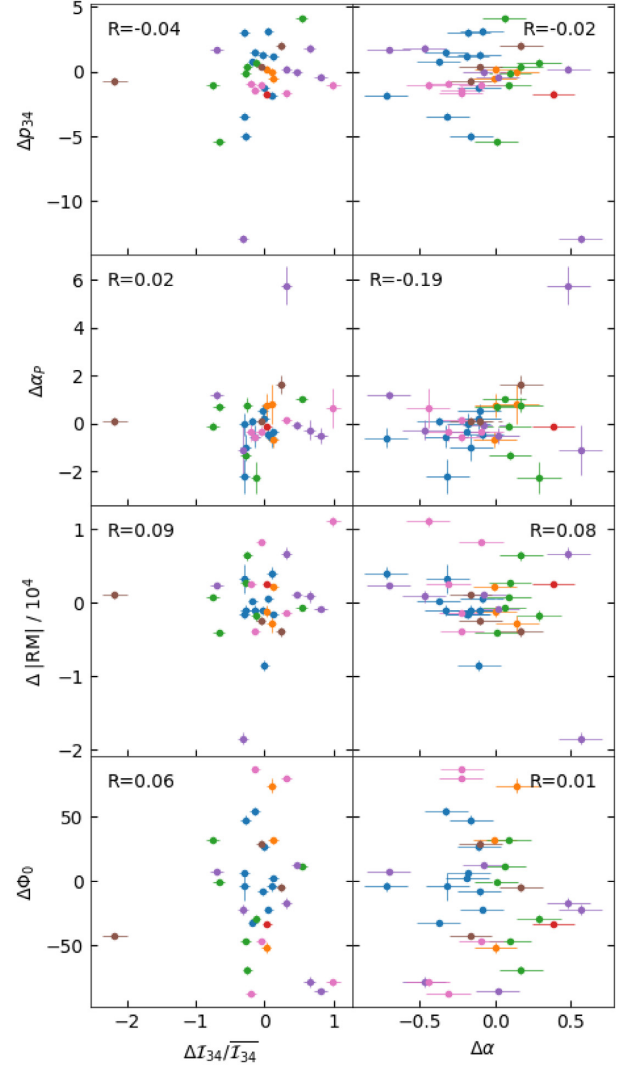


Figure 11. Correlations between total intensity flux density variation (left-hand column) and spectral index variation (right-hand column) with variability in the polarization parameters. Points are coloured by observing epoch as in Fig. 7.

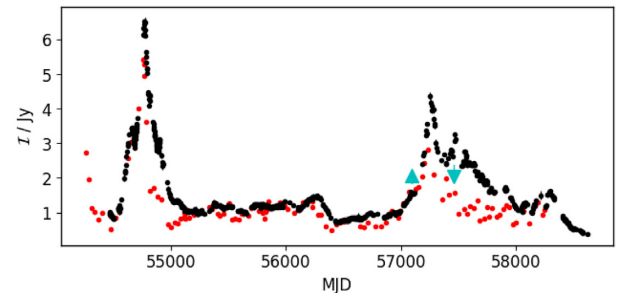


Figure 12. Light curves for PCCS1 G156.86–39.13 from OVRO at 15 GHz (black error bars); the VLBA at 43 GHz (red points) and the VLA observations (cyan lines from 28 to 40 GHz, with triangles at the 40-GHz end). See the text for more detail.

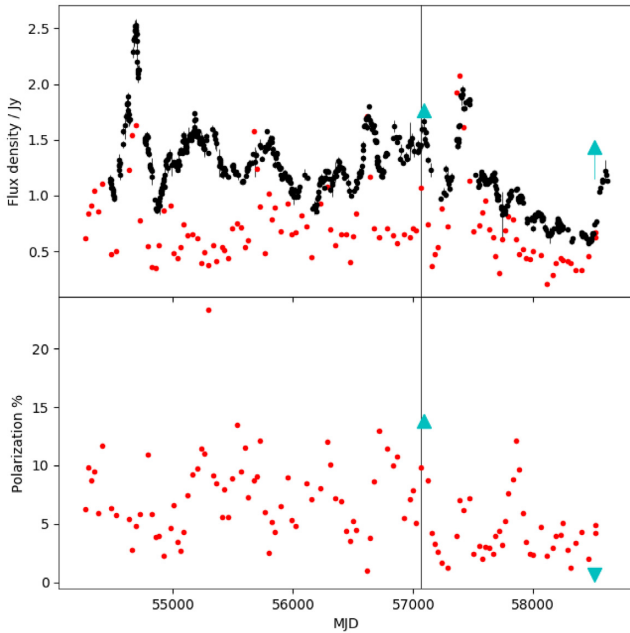


Figure 13. Light curves for PCCS1 G145.78+43.13 from OVRO at 15 GHz (black error bars); the VLBA at 43 GHz (red points) and the VLA observations (cyan lines from 28 to 40 GHz, with triangles at the 40-GHz end). The top panel shows total intensity while the bottom panel shows polarization fraction (in per cent). The vertical black line shows the date of the optical flare. See the text for more detail.

that may be a consequence of the rapid depolarization down to their lower frequencies (see Fig. 3). The intrinsic RM is larger than the intrinsic RM measured by Hovatta et al. (2019) for 3C 273 of $\approx 3.5 \times 10^4 \text{ rad m}^{-2}$ at $\approx 62 \text{ GHz}$ (extrapolating the measurement of $6.7 \times 10^5 \text{ rad m}^{-2}$ at observed wavelength $\approx 234 \text{ GHz}$ using $\text{RM}_{\text{int}} \propto \nu_{\text{em}}^2$) and $\approx 6 \times 10^4 \text{ rad m}^{-2}$ found for 3C 84 (extrapolating the measurement of $8.7 \times 10^5 \text{ rad m}^{-2}$ at observed wavelength $\approx 230 \text{ GHz}$) from Plambeck et al. (2014). It may even approach the current largest-known RM observed for the lensed quasar PKS 1830-211 Martí-Vidal et al. (2015), which is 10^8 rad m^{-2} at $\nu_{\text{em}} = 875\text{--}1050 \text{ GHz}$, corresponding to $4 \times 10^5 \text{ rad m}^{-2}$ at $\nu_{\text{em}} = 62 \text{ GHz}$ if the $\text{RM}_{\text{int}} \propto \nu_{\text{em}}^2$ law holds over such a wide range in frequency.

5.3 PCCS1 G145.78+43.13

PCCS1 G145.78+43.13 is a notable outlier in polarization fraction variation ($>46\sigma$). The total intensity and polarization fraction (in per cent) light curves for this source are shown in Fig. 13. It underwent an exceptionally high optical flare in 2015 (MJD = 57067), coinciding with the emergence of a new knot detected by the VLBA-BU-Blazar Monitoring Project (MAGIC Collaboration et al. 2018). Our first observing epoch of this source happened to coincide with the optical flare, and the polarization fraction measured at this epoch of 13.6 per cent agrees with the VLBA measurement of ≈ 10 per cent. In the most recent epoch, 2019 January 28, although the total intensity flux density as measured with the VLA has stayed relatively constant at $\approx 1.5 \text{ Jy}$, the total intensity spectral index has changed dramatically from $+0.06$ to $+0.62$; OVRO and VLBA monitoring data confirm that the source is undergoing a radio flare. The polarization fraction has decreased to 0.7 per cent, in line with the VLBA polarization values; the polarization fraction spectral index has steepened significantly from $+0.06$ to -0.92 ; and the RM has

significantly changed from -440 to $-18\,300 \text{ rad m}^{-2}$. These changes could be attributed to the integrated flux density during the flare state containing a significant contribution from the emerging knot of plasma.

6 IMPLICATIONS FOR QUIJOTE

As shown in, e.g. Battye et al. (2011) and Puglisi et al. (2018), polarized extra-galactic sources produce significant contamination to the B-mode power spectrum. The strong variability of the sources that dominate at the QUIJOTE frequencies that will be used for cosmological analysis means that care must be taken to correctly account for their presence.

Following the methodology described in Tucci & Toffolatti (2012), we now estimate the contribution of unresolved polarized radio sources to the angular power spectra at 30 GHz, and discuss the implications for that frequency channel of the QUIJOTE experiment. For a Poisson distribution of point sources with flux densities below a certain cut-off value S_C , the contribution to the B-mode angular power spectrum can be estimated as

$$C_\ell^{BB} = \frac{1}{2} \left(\frac{dB}{dT} \right)^{-2} \langle \Pi^2 \rangle \int_0^{S_C} n(S) S^2 dS, \quad (6)$$

where $n(S)$ is the differential number of sources per steradian, dB/dT is the conversion factor from brightness to temperature, and Π corresponds to the fractional polarization.

The model for the differential source counts is taken from de Zotti et al. (2005, 2010).⁵ The average value $\langle \Pi^2 \rangle$ can be computed using the fitted lognormal distribution function in Section 4.2, using the equations given in Battye et al. (2011) and Puglisi et al. (2018). In our case, we have $\sqrt{\langle \Pi^2 \rangle} \approx 3.3$ per cent.

At 30 GHz, we obtain $C_\ell^{BB} \approx 1.8 \times 10^{-4} \mu\text{K}^2$ for $S_C = 20 \text{ Jy}$, and $C_\ell^{BB} \approx 3.2 \times 10^{-5} \mu\text{K}^2$ for $S_C = 1 \text{ Jy}$. Fig. 14 shows this predicted contribution of radio sources at 30 GHz, as compared to the expected level of the primordial B-mode signal for values of the tensor-to-scalar ratio of $r = 0.2, 0.1$ and 0.05 . As an indication, we also include the prediction for $S_C = 0.3, 0.5$, and 0.1 Jy , assuming our polarization fraction results are valid down to these lower flux density limits; we emphasize however that a lower flux density limit would select a different population of sources (not necessarily blazars) and this may not be a valid extrapolation.

If we evaluate the contribution of radio sources to the total power in the BB spectrum at multipole $\ell = 80$ (i.e. close to the recombination bump of the expected cosmological signal), we find that the source contribution is reduced from 0.43 (for $S_C = 20 \text{ Jy}$) to $0.18 \mu\text{K}$ (for $S_C = 1 \text{ Jy}$). This level is comparable to the expected primordial B-mode signal for $r = 0.2$, consistently with the results presented in Rubiño-Martín et al. (2012, see their fig. 7) and Tucci et al. (2005). This highlights the importance of removing the contribution from these sources; since we find that both their total intensity and polarization vary unpredictably, it is likely that they will need to be masked in the analysis rather than subtracted directly, in the absence of simultaneous polarimetric monitoring observations.

Finally, the QUIJOTE experiment aims to reach a limit of $r = 0.1$ with measurements at 30 GHz made with the Thirty-GHz Instrument (TGI), and $r = 0.05$ when combining the TGI results with those from the Forty-GHz Instrument (Rubiño-Martín et al. 2012). As a reference, the best current constraints on tensor-to-scalar ratio

⁵ Available online http://w1.ira.inaf.it/rstools/srcnt/srcnt_tables.html.

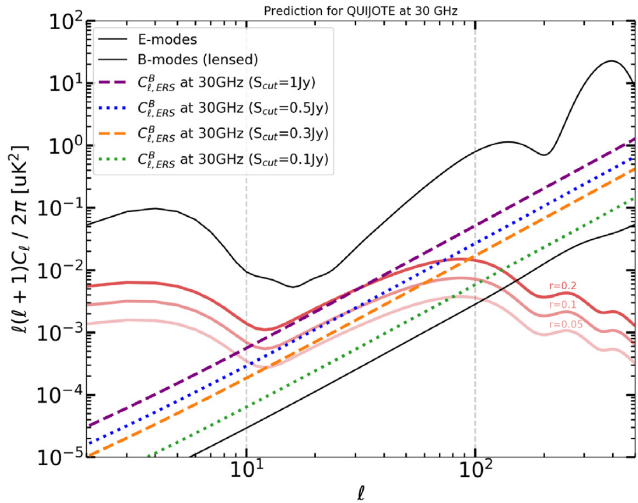


Figure 14. Predicted primordial E-mode signal (upper black line), lensing B-mode signal (lower black line), primordial B-mode signal depending on tensor-to-scalar ratio value (red and pink lines, labelled by r -value), and point source contamination depending on total intensity cut-off value (coloured dashed and dotted lines, as labelled in caption), all at 30 GHz. It can be seen that when masking sources with total intensity >1 Jy, a similar level of contamination to the $r = 0.2$ prediction is reached, while to reach $r = 0.05$, sources will likely need to be masked down to 100 mJy in total intensity.

are $r < 0.064$ (Planck Collaboration X 2020). This study suggests that we will need to remove sources down to ≈ 500 mJy in total intensity (see Fig. 14) to achieve the $r = 0.1$ limit with 30-GHz data only. And for the combined analysis of TGI and FGI data, we will possibly need to go below ≈ 300 mJy at 30 GHz in order to reach the $r = 0.05$ goal. However, more studies will need to be done on the source population at these lower flux densities to verify this. We also emphasize that these results are frequency-dependent and other experiments operating at different frequencies will be differently affected by point-source contamination.

7 CONCLUSIONS

In order to assess the contamination of the QUIJOTE cosmological fields by polarized emission from radio sources, we observed 51 sources, selected to be brighter than 1 Jy at 30 GHz, at 28–40 GHz with the VLA. The sample is dominated by flat-spectrum radio quasars. For 41 of the sources, we have two epochs of observation, which allows us to investigate the variability of the sources both in total intensity and polarization. We find the following:

- (i) Our in-band spectral indices agree well with simultaneously measured 15–34 GHz spectral indices using OVRO monitoring data, with some indication of spectral steepening at the higher band.
- (ii) The median polarization fraction of our sample at 34 GHz is 2.2 per cent, with the largest being 14 per cent; the distribution of polarization fractions agrees well with polarization fraction distributions at various frequencies summarized in Puglisi et al. (2018).
- (iii) We find a median RM of $|RM| \approx 1110$ rad m^{-2} , with one extreme outlier (4C 15.05) having $RM \approx -56\,000$ and $-64\,000$ rad m^{-2} in the two observation epochs. This may be amongst the highest RMs measured up to now in quasar cores.
- (iv) We find hints of a correlation between the total intensity flux density and the median polarization fraction; however, a larger sample complete to a lower flux density level would be required

to confirm this. We find no correlation between the total intensity spectral index of a source and its polarization fraction.

(v) Of the sources, 59 per cent are variable in total intensity, while all are variable in polarization at 3σ level. Changes in polarization fraction are roughly Gaussian-distributed with $\sigma = 1.8$ per cent, and one extreme outlier changes by 13 per cent.

(vi) We find no strong correlations between changes in polarization properties and changes in total intensity flux density or spectral index.

(vii) We conclude that due to these strong variations and lack of correlation, if high-cadence polarimetric monitoring observations of sources at similar frequency are not available, sources must be masked in the QUIJOTE analysis rather than subtracted. Assuming our results may be extrapolated to lower flux density source populations, sources above ≈ 300 mJy will need to be masked to reach the QUIJOTE goal of $r < 0.05$. For general experiments aiming to detect inflationary B modes, the point source population will need to be studied at the frequency of the experiment to determine the level of masking required.

ACKNOWLEDGEMENTS

We thank an anonymous reviewer who substantially improved the presentation of this paper. The QUIJOTE experiment is being developed by the Instituto de Astrofísica de Canarias (IAC), the Instituto de Física de Cantabria (IFCA), and the Universities of Cantabria, Manchester and Cambridge. Partial financial support is provided by the Spanish Ministry of Science, Innovation and Universities under the projects AYA2007-68058-C03-01, AYA2010-21766-C03-02, AYA2014-60438-P, AYA2017-84185-P, IACA13-3E-2336, IACA15-BE-3707, EQC2018-004918-P, the Severo Ochoa Program SEV-2015-0548, and also by the Consolider-Ingenio project CSD2010-00064 (EPI: Exploring the Physics of Inflation). This project has received funding from the European Union’s Horizon 2020 research and innovation program under grant agreement number 687312 (RADIOFOREGROUNDS). This publication makes use of data obtained at Metsähovi Radio Observatory, operated by Aalto University in Finland. This study makes use of 43-GHz VLBA data from the VLBA-BU Blazar Monitoring Program (VLBA-BU-BLAZAR; <http://www.bu.edu/blazars/VLBAproject.html>), funded by NASA through the Fermi Guest Investigator Program. The VLBA is an instrument of the National Radio Astronomy Observatory. The National Radio Astronomy Observatory is a facility of the National Science Foundation operated by Associated Universities, Inc. This research has made use of data from the OVRO 40-m monitoring program (Richards et al. 2011), which is supported in part by NASA grants NNX08AW31G, NNX11A043G, and NNX14AQ89G, and NSF grants AST-0808050 and AST-1109911. YCP is supported by a Trinity College JRF and a Rutherford Discovery Fellowship. FP acknowledges support from the Spanish Ministerio de Ciencia, Innovación y Universidades (MICINN) under grant numbers ESP2015-65597-C4-4-R, and ESP2017-86852-C4-2-R.

DATA AVAILABILITY

Raw data used in this study are publicly available from the VLA data archive (<https://archive.nrao.edu>) and can be accessed using the project codes in Table 3. Calibrated data are available on reasonable request from the authors.

REFERENCES

- Algaba J. C., Gabuzda D. C., Smith P. S., 2011, *MNRAS*, 411, 85
- Algaba J. C., Gabuzda D. C., Smith P. S., 2012, *MNRAS*, 420, 542
- Battye R. A., Browne I. W. A., Peel M. W., Jackson N. J., Dickinson C., 2011, *MNRAS*, 413, 132
- Bonavera L., González-Nuevo J., Argüeso F., Toffolatti L., 2017, *MNRAS*, 469, 2401
- de Vaucouleurs G., de Vaucouleurs A., Corwin H. G., Buta R. J., Paturel G., Fouque P., 1991, *Third Reference Catalogue of Bright Galaxies*. Springer, New York, NY, USA
- de Zotti G., Ricci R., Mesa D., Silva L., Mazzotta P., Toffolatti L., González-Nuevo J., 2005, *A&A*, 431, 893
- de Zotti G., Massardi M., Negrello M., Wall J., 2010, *A&ARv*, 18, 1
- Galluzzi V. et al., 2017, *MNRAS*, 465, 4085
- Galluzzi V. et al., 2018, *MNRAS*, 475, 1306
- Galluzzi V., Massardi M., 2016, *Int. J. Mod. Phys. D*, 25, 1640005
- Grainge K. et al., 2003, *MNRAS*, 341, L23
- Hales C. A., 2017, *CASA Interferometric Pipeline Polarization Calibration & Imaging Requirement & Design Specifications*, EVLA Memo Series, 201; also ALMA Memo Series, 603
- Hales C. A., 2017, *AJ*, 154, 54
- Hales C. A., 2017, Zenodo, record zenodo:801336
- Hovatta T. et al., 2012, *AJ*, 144, 105
- Hovatta T., O’Sullivan S., Martí-Vidal I., Savolainen T., Tchekhovskoy A., 2019, *A&A*, 623, A111
- Huchra J. P., Vogeley M. S., Geller M. J., 1999, *ApJS*, 121, 287
- Huffenberger K. M. et al., 2015, *ApJ*, 806, 112
- Jackson N., Browne I. W. A., Battye R. A., Gabuzda D., Taylor A. C., 2010, *MNRAS*, 401, 1388
- Jones T. W., Rudnick L., Aller H. D., Aller M. F., Hodge P. E., Fiedler R. L., 1985, *ApJ*, 290, 627
- Jorstad S. G. et al., 2007, *AJ*, 134, 799
- Kravchenko E. V., Cotton W. D., Kovalev Y. Y., 2015, in Massaro F., Cheung C. C., Lopez E., Siemiginowska A., eds, *Proc. IAU Symp. 313, Extragalactic Jets from Every Angle*. Kluwer, Dordrecht, p. 128
- Lister M. L., 2001, *ApJ*, 562, 208
- Liu H. B., Hasegawa Y., Ching T.-C., Lai S.-P., Hirano N., Rao R., 2018, *A&A*, 617, A3
- López-Caniego M., Massardi M., González-Nuevo J., Lanz L., Herranz D., De Zotti G., Sanz J. L., Argüeso F., 2009, *ApJ*, 705, 868
- MAGIC Collaboration et al., 2018, *A&A*, 617, A30
- Martí-Vidal I., Muller S., Vlemmings W., Horellou C., Aalto S., 2015, *Science*, 348, 311
- Massardi M. et al., 2008, *MNRAS*, 384, 775
- Massaro E., Maselli A., Leto C., Marchegiani P., Perri M., Giommi P., Piranomonte S., 2015, *Ap&SS*, 357, 75
- Meisner A. M., Romani R. W., 2010, *ApJ*, 712, 14
- O’Sullivan S. P. et al., 2012, *MNRAS*, 421, 3300
- Oriente M., Dallacasa D., 2008, *A&A*, 479, 409
- Park J. et al., 2018, *ApJ*, 860, 112
- Perley R. A., Butler B. J., 2013, *ApJS*, 206, 16
- Plambeck R. L. et al., 2014, *ApJ*, 797, 66
- Planck Collaboration X, 2020, *A&A*, 641, A10
- Planck Collaboration XLV, 2016, *A&A*, 596, A106
- Planck Collaboration XXVI, 2016, *A&A*, 594, A26
- Planck Collaboration XXVIII, 2014, *A&A*, 571, A28.
- Popescu C. C., Hopp U., Hagen H. J., Elsaesser H., 1996, *A&AS*, 116, 43
- Puglisi G. et al., 2018, *ApJ*, 858, 85
- Richards J. L. et al., 2011, *ApJS*, 194, 29
- Rubiño-Martín J. A. et al., 2010, *Astrophys. Space Sci. Proc.*, 14, 127
- Rubiño-Martín J. A. et al., 2012, in Clampin M. C., Fazio G. G., MacEwen H. A., Oschmann J. M., Jr., eds, *Proc. SPIE Conf. Ser. Vol. 8442, Space Telescopes and Instrumentation 2012: Optical, Infrared, and Millimeter Wave*. SPIE, Bellingham, p. SPIE.8444
- Rudnick L. et al., 1985, *ApJS*, 57, 693
- Sajina A., Partridge B., Evans T., Stefl S., Vechik N., Myers S., Dicker S., Korngut P., 2011, *ApJ*, 732, 45
- Schmidt M., 1965, *ApJ*, 141, 1
- Terasranta H. et al., 1992, *A&AS*, 94, 121
- Trager S. C., Faber S. M., Worthey G., González J. J., 2000, *AJ*, 119, 1645
- Tucci M., Toffolatti L., 2012, *Adv. Astron.*, 2012, 624987
- Tucci M., Martínez-González E., Vielva P., Delabrouille J., 2005, *MNRAS*, 360, 935
- Zavala R. T., Taylor G. B., 2004, *ApJ*, 612, 749

SUPPORTING INFORMATION

Supplementary data are available at *MNRAS* online.

appendix_r3-compressed.pdf
Table4_full_r2.txt

Please note: Oxford University Press is not responsible for the content or functionality of any supporting materials supplied by the authors. Any queries (other than missing material) should be directed to the corresponding author for the article.

This paper has been typeset from a $\text{\TeX}/\text{\LaTeX}$ file prepared by the author.